

# Amorphous MoS<sub>2</sub>/MoO<sub>3</sub> Nanosheets as High-Efficient Polysulfide Barrier in Li–S Batteries

Min Qing,<sup>[a]</sup> Zhi Hui Hao,<sup>[a]</sup> Xiangwei Zhao,<sup>[a]</sup> Qin Dong,<sup>[a]</sup> Zhimin He,<sup>[a]</sup> Wei Hong,<sup>\*[a]</sup> and Rong Li<sup>\*[a]</sup>

Lithium-sulfur batteries (LSBs) are seriously impeded by poor reaction kinetics and the polysulfides shuttling, leading to low utilization of sulfur and poor cycling performance. Herein, amorphous MoS<sub>2</sub>/MoO<sub>3</sub> nanosheets are prepared by a one-step formamide (FA)-assisted strategy. Due to the merits of high adsorption capability and good catalytic activity of MoS<sub>2</sub>, relatively high electronic conductivity and strong polarity of

MoO<sub>3</sub>, and abundant active sites of amorphous nanosheet structure, the LSBs based on amorphous MoS<sub>2</sub>/MoO<sub>3</sub>-2 nanosheets coated separator exhibit an outstanding specific capacity (1420.2 mA h g<sup>-1</sup> at 0.1 C), excellent rate capacity (505.4 mA h g<sup>-1</sup> at 5 C), and long cycle life (a negligible decay rate of 0.063% per cycle at 0.5 C). This work provides an idea for designing efficient amorphous catalytic materials in LSBs.

## Introduction

With the growing market of portable devices and electric vehicles, the demand for rechargeable batteries with low cost, high power density, environmental benignancy and long cycle life is increasing.<sup>[1–3]</sup> Lithium-sulfur batteries (LSBs) serve well as ideal candidates for next-generation batteries due to their high theoretical specific capacity (1675 mA h g<sup>-1</sup>), theoretical energy density (2600 Wh kg<sup>-1</sup>), and earth abundance of S.<sup>[4–7]</sup> Nevertheless, the commercialization of LSBs is strictly limited by some challenges to the sulfur cathode, such as large volume fluctuation during cycling, the poor electrical conductivity of S, and the lithium polysulfides (LiPSs) shuttling.<sup>[8–10]</sup> Among them, the LiPSs shuttling, where the LiPSs migrate to the lithium anode and are irreversibly reacted with lithium to form an insoluble Li<sub>2</sub>S layer on the anode electrode surface, leading to low Coulombic efficiency and the lithium anode corrosion, considered to be the most challenging issue.<sup>[11]</sup> Therefore, solving the shuttle of LiPSs is the key point for practical use of LSBs.

So far, many strategies have been employed to prevent the shuttling of soluble LiPSs. Among them, separator modification is one of the most effective methods. Non-polar carbon-based nanomaterials, such as carbon nanotubes,<sup>[12]</sup> porous carbon,<sup>[13–15]</sup> and graphene<sup>[16,17]</sup> have been widely used to be coated on separator to trap the polar polysulfides. However, the weak physical absorbability of carbon materials for polysulfides leaded to limited success. Polar materials, such as TiO<sub>2</sub>,<sup>[18]</sup> are alternative separator modifiers, which can confine the polysulfides via strong chemical adsorption. Nevertheless, chemical

adsorption strategies can only alleviate the shuttle problem to a certain extent, but it is still far from satisfactory.

Introducing a catalyst as separator modifier in the LSBs has been considered as a more effective approach to limit the LiPSs shuttling, which can reduce dissolvable LiPSs accumulation in the electrolyte by enhancing the redox kinetics of LiPSs. Transition metal compounds, such as metal nitrides,<sup>[19–21]</sup> metal sulfides,<sup>[22–26]</sup> metal oxides<sup>[27–30]</sup> have been widely studied as catalysts for LiPSs conversions in LSBs. Two-dimensional (2D) MoS<sub>2</sub> nanosheets have been proposed to be a promising candidate, which can not only anchor LiPSs through dipolar interaction of Mo–S bonds and strong S–S interaction, but also has good catalytic activity for LiPSs conversion.<sup>[31,32]</sup> For instance, Tang fabricated a thin layer of MoS<sub>2</sub> as a separator modifier for LSBs, alleviating the polysulfide shuttling and improving reaction kinetics.<sup>[33]</sup> Li prepared MoS<sub>2</sub>/C microsphere used as a functional separator, delivering an high initial capacity of 935 mA h g<sup>-1</sup> at 1.0 C and maintaining a capacity of 494 mA h g<sup>-1</sup> after 1000 cycles.<sup>[34]</sup> Unfortunately, the MoS<sub>2</sub> has poor conductivity, which limits its catalytic efficiency.<sup>[35]</sup> The 2D layered structure of MoO<sub>3</sub>, composed of MoO<sub>6</sub> octahedra, has attracted extensive research in various fields, including photo- and electrocatalysis,<sup>[36–38]</sup> supercapacitors,<sup>[39,40]</sup> and Li-ion batteries.<sup>[41,42]</sup> MoO<sub>3</sub> has strong polarity, high chemical stability and relatively higher conductivity than MoS<sub>2</sub>.<sup>[43]</sup> Incorporating MoS<sub>2</sub> with MoO<sub>3</sub> can offer a synergistic effect, which can enhance the conductivity, polarity and stability of MoS<sub>2</sub>, and thus provide better catalytic activity and stability.

Compared to crystalline materials, amorphous materials possess more crystalline defects, which are favorable for providing adequate active sites to anchor and catalyze LiPSs to suppress LiPSs shuttling.<sup>[44]</sup> Therefore, the amorphous materials coated on separators can effectively enhance the performance of the LSBs.

Herein, we reported a one-step formamide (FA)-assisted method to prepare amorphous MoS<sub>2</sub>/MoO<sub>3</sub> nanosheets. The synergistic effects of MoO<sub>3</sub> and MoS<sub>2</sub> can improve the adsorption capability and catalytic effect of LiPSs, and the

[a] M. Qing, Z. H. Hao, X. Zhao, Q. Dong, Z. He, W. Hong, R. Li  
Chemical Synthesis and Pollution Control Key Laboratory of Sichuan Province, College of Chemistry and Chemical Engineering, China West Normal University, Nanchong 637000, China  
E-mail: hongwei@cwnu.edu.cn  
lirong406b@126.com

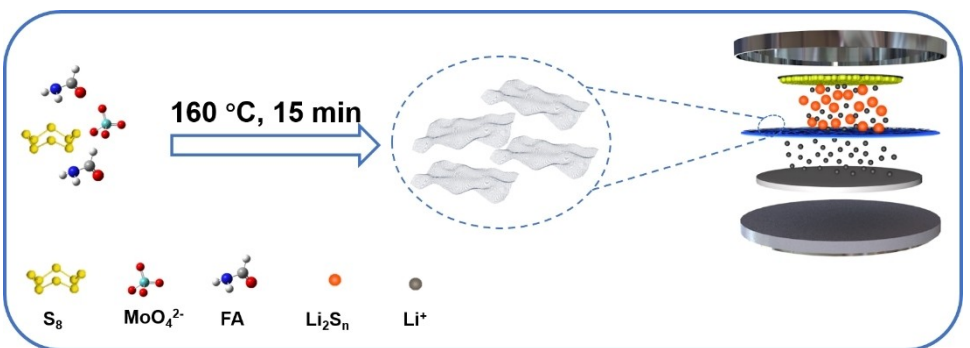
 Supporting information for this article is available on the WWW under <https://doi.org/10.1002/batt.202400089>

amorphous structure can also enhance LiPSs adsorption and increase catalytic sites, which improve the redox kinetics of LiPSs. Hence, the LSBs based on MoS<sub>2</sub>/MoO<sub>3</sub>-2 composite coated separators exhibit an excellent specific capacity, superior rate capacity, and long cycle life. Furthermore, the battery shows a high capacity at high S loading. This work provides an idea for designing efficient amorphous catalytic materials in LSBs.

## Results and Discussion

The preparation procedure of amorphous MoS<sub>2</sub>/MoO<sub>3</sub> nanosheets is presented in Scheme 1. The MoS<sub>2</sub>/MoO<sub>3</sub> nanosheets were produced through a one-step FA-assisted strategy using FA as the solvent, (NH<sub>4</sub>)<sub>6</sub>Mo<sub>7</sub>O<sub>24</sub> and S powder as precursors. The SEM image of the obtained MoS<sub>2</sub>/MoO<sub>3</sub>-2 was presented in

Figure S1. It showed a sheetlike morphology. From the TEM images in Figure 1a, sheetlike structures of MoS<sub>2</sub>/MoO<sub>3</sub>-2 were also observed, which were in good agreement with the SEM observation. The High-resolution (HR-TEM) images (Figure 1b) of MoS<sub>2</sub>/MoO<sub>3</sub>-2 showed no distinct lattice, and the selected area electron diffraction (SAED) image showed hazy haloes (Figure 1c), indicating the amorphous nature of the MoS<sub>2</sub>/MoO<sub>3</sub>-2 nanosheets. The high-angle annular dark-field scanning TEM (HAADF-STEM) and elemental mapping images indicated the uniform distribution of Mo, O and S elements in the MoS<sub>2</sub>/MoO<sub>3</sub> nanosheets (Figure 1d). The amorphous feature of MoS<sub>2</sub>/MoO<sub>3</sub> samples was further verified by XRD patterns. As displayed in Figure 1e, the MoS<sub>2</sub>/MoO<sub>3</sub> nanosheets had no obvious diffraction peaks, suggesting their amorphous feature. For comparison, the crystalline MoS<sub>2</sub>/MoO<sub>3</sub> was also synthesized according to a previous report.<sup>[45]</sup> The diffraction peaks of crystalline MoS<sub>2</sub>/MoO<sub>3</sub>, as shown in Figure S2, matched well



Scheme 1. Schematic illustration of the rapid preparation of amorphous MoS<sub>2</sub>/MoO<sub>3</sub> nanosheets.

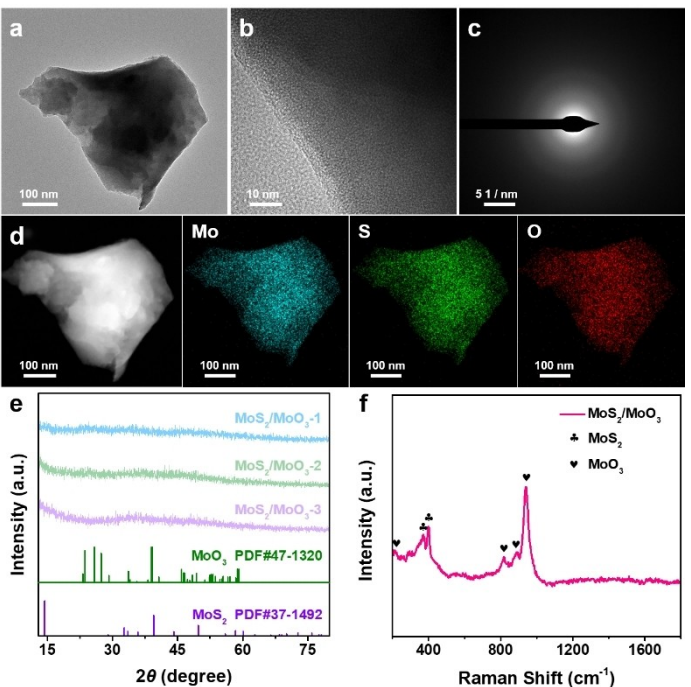


Figure 1. TEM image (a), HRTEM image (b), SAED image (c), HAADF image and corresponding EDS mapping images (d), Raman spectra (f) of MoS<sub>2</sub>/MoO<sub>3</sub>-2. XRD profile of different MoS<sub>2</sub>/MoO<sub>3</sub> samples (e).

with the phases of  $\text{MoO}_3$  (PDF#47-1320) and  $\text{MoS}_2$  (PDF#37-1492), suggesting the formation of both  $\text{MoS}_2$  and  $\text{MoO}_3$  in crystalline  $\text{MoS}_2/\text{MoO}_3$ . Raman spectra were used to elucidate the composition of  $\text{MoS}_2/\text{MoO}_3$ -2 nanosheets (Figure 1f). The peaks located at 371 and 401  $\text{cm}^{-1}$  corresponded to the  $E_{2g}^1$  and  $A_{1g}$  mode of  $\text{MoS}_2$ <sup>[46]</sup> while the peaks at 198 and 886  $\text{cm}^{-1}$  were related to  $\text{O}=\text{Mo}=\text{O}$  twisting and stretch of terminal oxygen atom vibration modes of  $\text{MoO}_3$ , respectively.<sup>[47,48]</sup> In addition, the other two peaks at 821 and 938  $\text{cm}^{-1}$  were attributed to terminal  $\text{M}=\text{O}$  stretching.<sup>[49,50]</sup> The surface chemistry of  $\text{MoS}_2/\text{MoO}_3$  samples were further analyzed by XPS. The survey spectra showed the existence of Mo, S, O, and C elements in all samples, as displayed in Figure 2a. The Mo 3d spectrum of  $\text{MoS}_2/\text{MoO}_3$  could be divided into two doublets (Figure 2b), attributing to  $\text{Mo}^{6+}3\text{d}_{5/2}/\text{Mo}^{6+}3\text{d}_{3/2}$  of  $\text{MoO}_3$  and  $\text{Mo}^{4+}3\text{d}_{5/2}/\text{Mo}^{4+}3\text{d}_{3/2}$  of  $\text{MoS}_2$ ,<sup>[45]</sup> respectively. Similarly, S 2p spectra could be divided into two peaks, belonging to the S 2p<sub>1/2</sub> and S 2p<sub>3/2</sub> orbitals of  $\text{S}^{2-}$  in  $\text{MoS}_2$  (Figure 2c).<sup>[51]</sup> All these results confirm that the  $\text{MoS}_2$  and  $\text{MoO}_3$  coexist in  $\text{MoS}_2/\text{MoO}_3$ -2 nanosheets. As shown in Figure 2d, the O 1s spectra showed three peaks, which corresponded to adsorbed water, the surface  $\text{OH}^-$  and metal oxygen.<sup>[52,53]</sup> With increasing the ratio of  $(\text{NH}_4)_6\text{Mo}_7\text{O}_{24}$ , the content of  $\text{MoO}_3$  increased, and the Mo 3d and S 2p peaks (Table S1) shifted to a higher binding energy, while O 1s peaks shifted to a lower binding energy, which suggest that electron transfer occurs between  $\text{MoO}_3$  and  $\text{MoS}_2$ .<sup>[54]</sup>

The  $\text{Li}_2\text{S}_6$  adsorption experiments of the samples were performed to evaluate the LiPSs adsorption ability. The  $\text{Li}_2\text{S}_6$  solution containing  $\text{MoS}_2/\text{MoO}_3$ -2 was almost colorless after a 24 h adsorption, superior to that of  $\text{MoS}_2/\text{MoO}_3$ -1 and  $\text{MoS}_2/\text{MoO}_3$ -3 turning to light yellow, as displayed in Figure 3a. As shown in UV-vis spectra (Figure 3b), the  $\text{Li}_2\text{S}_6$  absorption peak of  $\text{MoS}_2/\text{MoO}_3$ -2 was weaker than  $\text{MoS}_2/\text{MoO}_3$ -3 and  $\text{MoS}_2/\text{MoO}_3$ -1. These results indicated that  $\text{MoS}_2/\text{MoO}_3$ -2 had a higher chemical adsorption capacity for LiPSs compared to the  $\text{MoS}_2/\text{MoO}_3$ -3 and  $\text{MoS}_2/\text{MoO}_3$ -1. A diffusion measurement was further conducted to visually the LiPSs adsorption ability of different samples. As shown in Figure 3c, the solution in the big bottle with PP separator changed from colorless to yellow after resting 6 h, while for  $\text{MoS}_2/\text{MoO}_3$ -2 modified separators, the solution was still almost unchanged even after 12 h, indicating that  $\text{MoS}_2/\text{MoO}_3$ -2 had an outstanding hindrance to the LiPSs diffusion. As shown in Figure 4a, the  $\text{MoS}_2/\text{MoO}_3$ -2 modified separator remained foldable and flexible, with no powder peeling-off even after bending, suggesting a good adhesion between the composite and the PP separator. The SEM images displayed that the surface of  $\text{MoS}_2/\text{MoO}_3$ -2 modified separator were uniformly coated by the  $\text{MoS}_2/\text{MoO}_3$ -2 nanosheets, and clearly different from that of pristine PP separator (Figure 4b and c). In addition,  $\text{MoS}_2/\text{MoO}_3$ -2 modified separator showed a smaller electrolyte contact angle ( $0^\circ$ ) than PP ( $40.3^\circ$ ),  $\text{MoS}_2/\text{MoO}_3$ -1 ( $5.9^\circ$ ) and  $\text{MoS}_2/\text{MoO}_3$ -3 ( $6.4^\circ$ ) (Figure 4d-g) modified separators, suggesting its remarkable electrolyte affinity, which contributed to the adsorption of LiPSs.

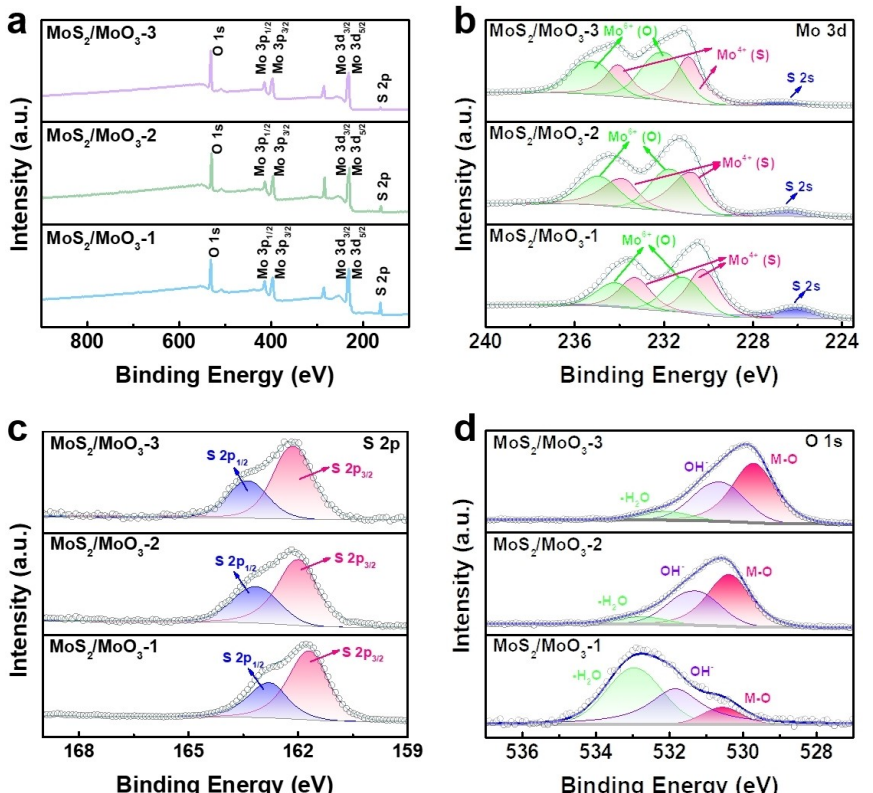
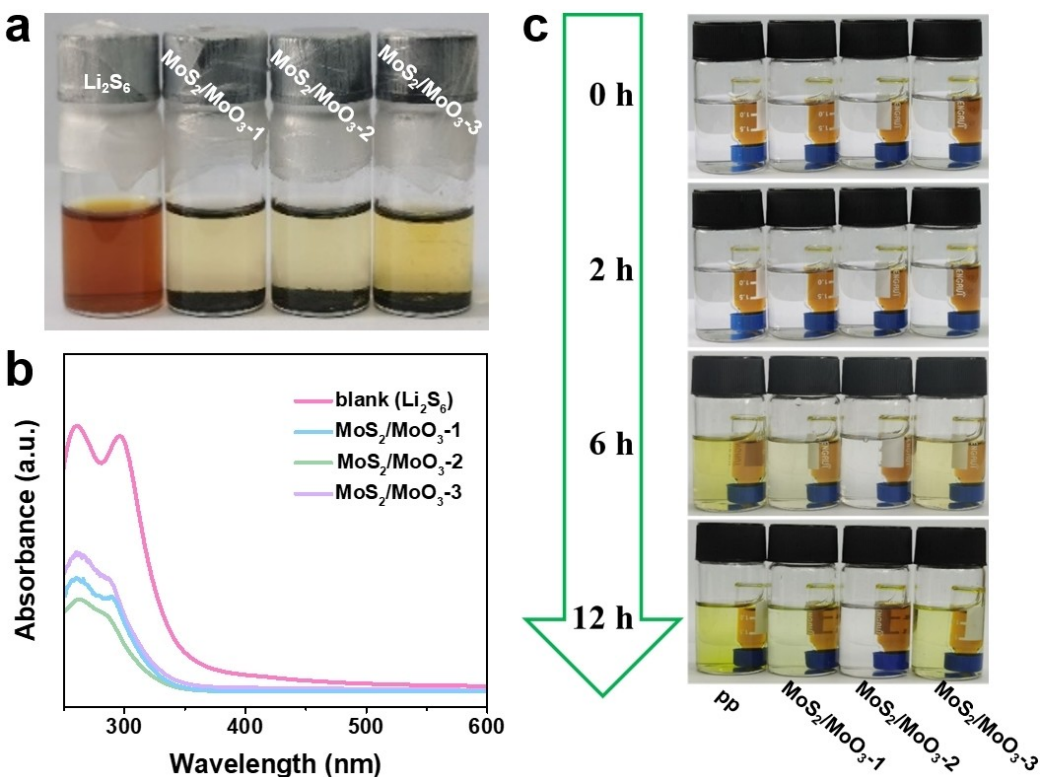
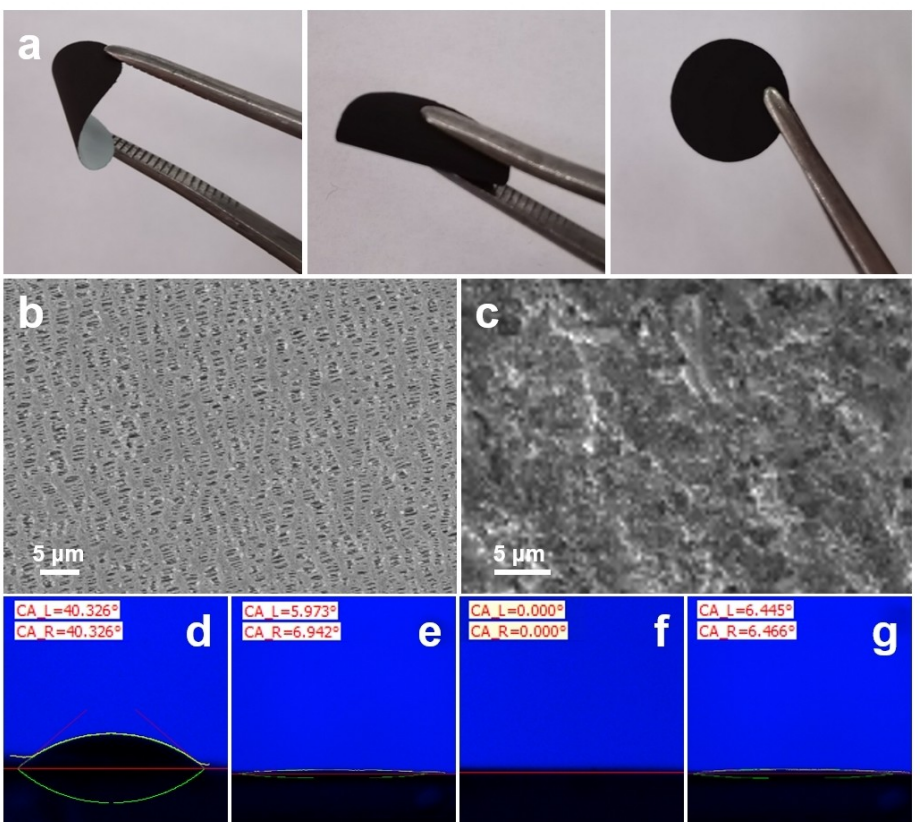


Figure 2. XPS spectra of survey spectrum (a), high-resolution Mo 3d (b), S 2p (c) and O 1s (d) spectrum of different  $\text{MoS}_2/\text{MoO}_3$  nanosheets.



**Figure 3.** Digital photograph of Li<sub>2</sub>S<sub>6</sub> absorption experiment (a), and the corresponding UV-vis absorption spectra for the different MoS<sub>2</sub>/MoO<sub>3</sub>. (c) The permeation test of polysulfides with PP and different MoS<sub>2</sub>/MoO<sub>3</sub> coated separators.



**Figure 4.** Digital photographs of flexible test for MoS<sub>2</sub>/MoO<sub>3</sub>-2 coated PP separator. SEM images of pristine separator (b) and MoS<sub>2</sub>/MoO<sub>3</sub>-2-coated separator (c). Contact angles between pristine separator (d), MoS<sub>2</sub>/MoO<sub>3</sub>-1 (e), MoS<sub>2</sub>/MoO<sub>3</sub>-2 (f), MoS<sub>2</sub>/MoO<sub>3</sub>-3 (g) modified separators and electrolyte.

The EIS was performed to evaluate the  $\text{Li}^+$  transport capacity of the batteries with different modified separators (Figure S3). When absorbing the electrolyte reached to saturation, the  $\text{Li}^+$  conductivity value for  $\text{MoS}_2/\text{MoO}_3\text{-2}$  modified separator ( $0.48 \text{ mS cm}^{-1}$ ) was close to that of pure separators ( $0.55 \text{ mS cm}^{-1}$ ) (Table S2), suggesting that coating the  $\text{MoS}_2/\text{MoO}_3\text{-2}$  interlayer did not impede the  $\text{Li}^+$  conduction. In order to investigate the liquid-liquid conversion redox kinetics, cyclic voltammetry (CV) tests were performed in symmetrical cells. As displayed in Figure S4, the  $\text{MoS}_2/\text{MoO}_3\text{-2}$  showed the highest current response, suggesting effectively accelerated the reaction kinetics for LiPSs conversion.

$\text{Li}_2\text{S}$  precipitation and dissolution tests on the LSBs with different samples modified separators were conducted to compare the ability of catalyze  $\text{Li}_2\text{S}$  precipitation and dissolution process. As displayed in Figure 5a–c,  $\text{MoS}_2/\text{MoO}_3\text{-2}$  based battery showed a shorter conversion time and higher deposition capacity ( $988 \text{ s}$ ,  $229 \text{ mAh g}^{-1}$ ) than those of  $\text{MoS}_2/\text{MoO}_3\text{-1}$  ( $1180 \text{ s}$ ,  $157.3 \text{ mAh g}^{-1}$ ) and  $\text{MoS}_2/\text{MoO}_3\text{-3}$  ( $1865 \text{ s}$ ,  $129.8 \text{ mAh g}^{-1}$ ). As presented in Figure 5d–f, the  $\text{MoS}_2/\text{MoO}_3\text{-2}$  based battery displayed a relatively higher  $\text{Li}_2\text{S}$  decomposition capacity of  $221.4 \text{ mAh g}^{-1}$  in comparison with  $\text{MoS}_2/\text{MoO}_3\text{-1}$  ( $188.5 \text{ mAh g}^{-1}$ ) and  $\text{MoS}_2/\text{MoO}_3\text{-3}$  ( $127.9 \text{ mAh g}^{-1}$ ). These results indicated that the  $\text{MoS}_2/\text{MoO}_3\text{-2}$  not only can catalyze  $\text{Li}_2\text{S}$  precipitation but also decomposition process, so as to speed up solid-liquid conversion kinetics of LiPSs.

The electrochemical performance of the LSBs using different  $\text{MoS}_2/\text{MoO}_3$  nanosheets coated separators and the pristine separator were tested with S loading of  $1.2 \text{ mg cm}^{-2}$ . The CV curve of  $\text{MoS}_2/\text{MoO}_3\text{-2}$  showed two reduction peaks at  $2.33$  and  $2.06 \text{ V}$ , corresponding to the reduction process from  $\text{S}_8$  to soluble long-chain LiPSs ( $\text{Li}_2\text{S}_x$ ,  $4 \leq x \leq 8$ ), further to  $\text{Li}_2\text{S}_2$  and  $\text{Li}_2\text{S}$  (Figure 6a). The CV curve of the  $\text{MoS}_2/\text{MoO}_3\text{-2}$  displayed one anodic peak at  $2.41 \text{ V}$ , which contributed to the conversion from  $\text{Li}_2\text{S}_2$  and  $\text{Li}_2\text{S}$  to  $\text{S}_8$ . The potential separation between

reduction (peak B) and oxidation (peak C) peaks for  $\text{MoS}_2/\text{MoO}_3\text{-2}$  was smaller than that in the  $\text{MoS}_2/\text{MoO}_3\text{-1}$ ,  $\text{MoS}_2/\text{MoO}_3\text{-3}$  and PP, indicating much faster reaction kinetics in  $\text{MoS}_2/\text{MoO}_3\text{-2}$ . The initial five CV curves of LSBs with pristine separator and  $\text{MoS}_2/\text{MoO}_3$  modified separators were shown in Figure S5. The intensity and position of oxidation and reduction peaks for pristine separator displayed distinct change in subsequent four cycles. However, the intensity and position of peaks for different  $\text{MoS}_2/\text{MoO}_3$  modified separators showed well-overlapped in subsequent cycles, indicating high reversibility and cycle stability.

The  $\text{Li}^+$  diffusion coefficient ( $D_{\text{Li}^+}$ ) was calculated using the Randles-Sevcik equation.<sup>[55]</sup> As shown in Figure S6e–g, the slopes of the batteries with  $\text{MoS}_2/\text{MoO}_3$  coated separators were larger than those of pristine separator, and the  $D_{\text{Li}^+}$  values for  $\text{S}_8$  to soluble long-chain LiPSs, LiPSs to  $\text{Li}_2\text{S}_2/\text{Li}_2\text{S}$ ,  $\text{Li}_2\text{S}_2/\text{Li}_2\text{S}$  to  $\text{S}_8$  on  $\text{MoS}_2/\text{MoO}_3\text{-2}$  coated separators were always larger than that of  $\text{MoS}_2/\text{MoO}_3\text{-1}$ ,  $\text{MoS}_2/\text{MoO}_3\text{-3}$  coated separators and the pristine separator (Figure S6h), indicating faster  $\text{Li}^+$  diffusion coefficient.

The discharge/charge profiles of the LSBs with different  $\text{MoS}_2/\text{MoO}_3$  coated separators and the pristine separator were shown in Figure 6b. The profiles had one charge plateau and two discharge plateaus, which is consistent with the CV curves. The battery with pristine separator demonstrated an initial discharge specific capacity of  $567 \text{ mAh g}^{-1}$  at  $0.5 \text{ C}$ . However, the capacities of  $\text{MoS}_2/\text{MoO}_3\text{-1}$ ,  $\text{MoS}_2/\text{MoO}_3\text{-2}$  and  $\text{MoS}_2/\text{MoO}_3\text{-3}$  coated separators increased to  $1010.8$ ,  $1158.2$  and  $944.3 \text{ mAh g}^{-1}$ , respectively, suggesting the higher sulfur utilization rate. In particular, the polarization voltage ( $\Delta E$ ) for batteries with  $\text{MoS}_2/\text{MoO}_3\text{-2}$  coated separator ( $0.195 \text{ V}$ ) is smaller than that of  $\text{MoS}_2/\text{MoO}_3\text{-1}$  ( $0.202 \text{ V}$ ),  $\text{MoS}_2/\text{MoO}_3\text{-3}$  ( $0.235 \text{ V}$ ) coated separator and pristine separator ( $0.247 \text{ V}$ ). This result indicated that the  $\text{MoS}_2/\text{MoO}_3\text{-2}$  reduced the redox polarization in the LSBs. Moreover, the battery with  $\text{MoS}_2/\text{MoO}_3\text{-2}$  coated separator

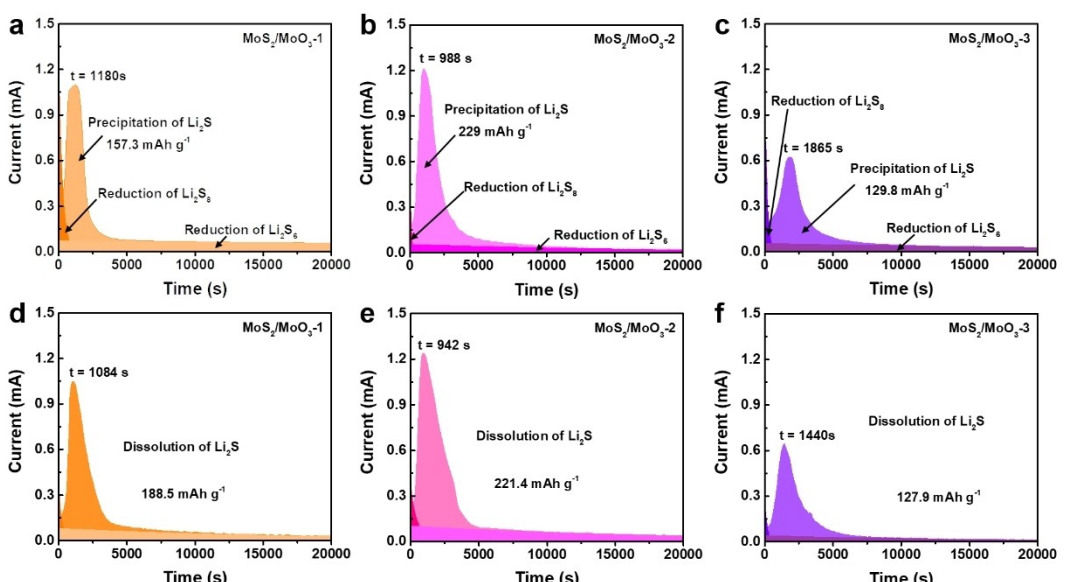
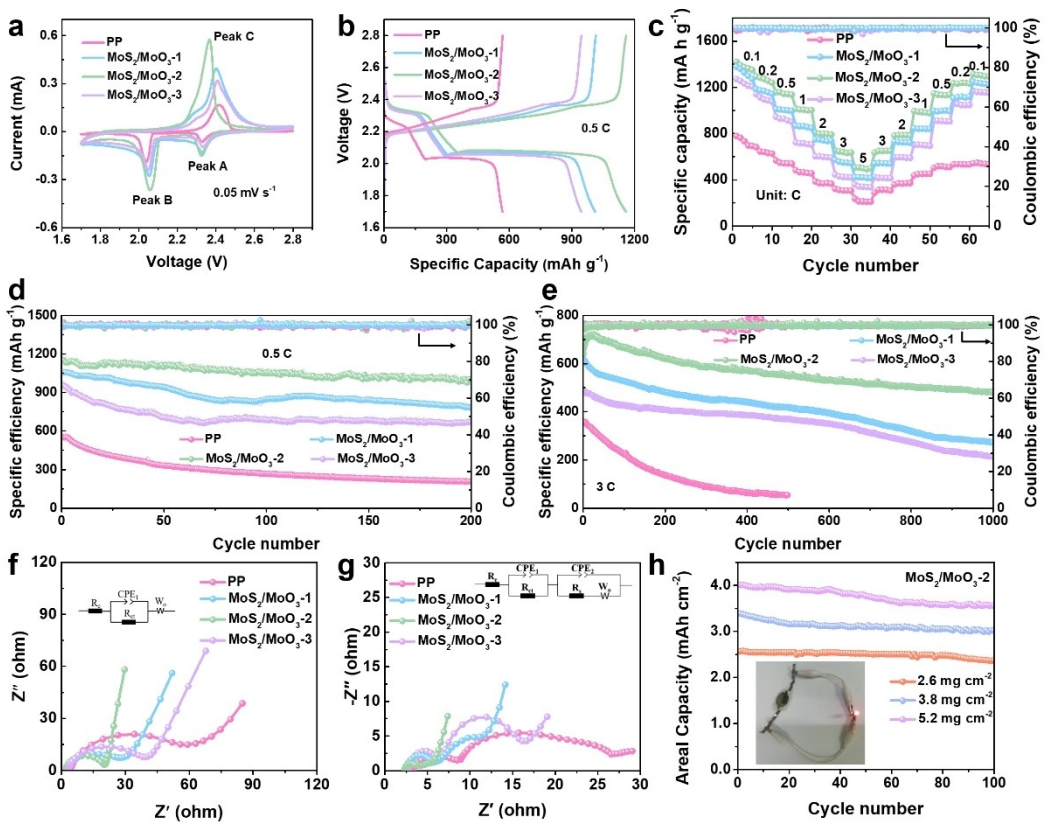


Figure 5. Potentiostatic discharge curves at  $2.02 \text{ V}$  (a–c) and charge curves at  $2.4 \text{ V}$  (d–f) for the batteries with different  $\text{MoS}_2/\text{MoO}_3$  coated separators.



**Figure 6.** The electrochemical performance of the LSBs based on different separators. CV curves in the voltage range of 1.7–2.8 V at  $0.05 \text{ mV s}^{-1}$  (a). The first charge/discharge curves at  $0.5 \text{ C}$  (b). The rate capability from  $0.1$  to  $5 \text{ C}$  (c). Cycling performance at  $0.5 \text{ C}$  (d) and  $3 \text{ C}$  (e). Nyquist plots before (f) and after 200 cycles (g) at  $0.5 \text{ C}$ . Cycling performance of the batteries with  $\text{MoS}_2/\text{MoO}_3$ -2 modified separator under different sulfur loadings ( $2.6$ ,  $3.8$  and  $5.2 \text{ mg cm}^{-2}$ ) at  $0.5 \text{ C}$  (h). Inset: digital picture of LED light powered by the coin battery with sulfur loading of  $2.6 \text{ mg cm}^{-2}$ .

showed the largest capacity of  $813.7 \text{ mAh g}^{-1}$  than  $\text{MoS}_2/\text{MoO}_3$ -1 ( $698.2 \text{ mAh g}^{-1}$ ) and  $\text{MoS}_2/\text{MoO}_3$ -3 ( $649.1 \text{ mAh g}^{-1}$ ) at the lower discharge plateau (ca.  $2.1 \text{ V}$ ), which indicated the high conversion rate from  $\text{Li}_2\text{S}_4$  to  $\text{Li}_2\text{S}/\text{Li}_2\text{S}$ . When compared with crystalline  $\text{MoS}_2/\text{MoO}_3$  (Figure S7), the  $\text{MoS}_2/\text{MoO}_3$ -2 coated separator still showed a higher initial discharge capacity and smaller polarization voltage. As displayed in Figure 6c, the rate performance displayed that  $\text{MoS}_2/\text{MoO}_3$ -2 exhibited the capacities of  $1420.2$ ,  $1295$ ,  $1158.2$ ,  $1015$ ,  $806.7$ ,  $650.3$  and  $504.2 \text{ mAh g}^{-1}$  at  $0.1$ ,  $0.2$ ,  $0.5$ ,  $1$ ,  $2$ ,  $3$  and  $5 \text{ C}$ , respectively. When the current changed from  $5$  to  $0.1 \text{ C}$ , the capacity of battery with  $\text{MoS}_2/\text{MoO}_3$ -2 coated separator could still reach  $1315 \text{ mAh g}^{-1}$ , suggesting the superior stability of the  $\text{MoS}_2/\text{MoO}_3$ -2. The corresponding charge/discharge profiles and polarization voltage of these batteries at different rate were shown in Figure S8 and S9. It could be seen that the  $\text{MoS}_2/\text{MoO}_3$ -2 based battery displayed the best rate capability and smallest polarization voltage.

The Tafel plots were also calculated according to linear sweep voltammetry (LSV) (Figure S10). The batteries with the  $\text{MoS}_2/\text{MoO}_3$ -2 coated separators displayed the smallest slope during both the anodic ( $116.24 \text{ mV dec}^{-1}$ ) and cathodic ( $41.33 \text{ mV dec}^{-1}$ ) processes, suggesting the effectively improved the reaction kinetics for the LiPSs conversion, which could be ascribed to the excellent electrocatalytic effect of the  $\text{MoS}_2$  and

$\text{MoO}_3$  in  $\text{MoS}_2/\text{MoO}_3$ -2. The activation energy ( $E_a$ ) of the discharge process was then calculated from the Tafel plots.<sup>[56]</sup> The equation used was given in the Supporting Information. The  $E_a$  values for  $\text{MoS}_2/\text{MoO}_3$ -2 were dramatically reduced by  $60.27 \text{ kJ mol}^{-1}$  for the reactions from  $\text{S}_8$  to  $\text{Li}_2\text{S}_n$  and  $56.57 \text{ kJ mol}^{-1}$  for  $\text{Li}_2\text{S}_n$  to  $\text{Li}_2\text{S}$  (Figure S11), confirming enhanced LiPSs conversion rate.

The long-term cyclic performance of LSBs with different  $\text{MoS}_2/\text{MoO}_3$  nanosheets coated separators and the pristine separator were tested. The battery with  $\text{MoS}_2/\text{MoO}_3$ -2 coated separators presented a capacity of  $1005 \text{ mAh g}^{-1}$  with a low capacity decay rate of  $0.063\%$  per cycle at  $0.5 \text{ C}$  after 200 cycles (Figure 6d). While, the LSBs with pristine separator exhibited a lower capacity of  $550 \text{ mAh g}^{-1}$  and the capacity decay sharply with higher decay rate of  $0.15\%$  per cycle after 200 cycles. In addition, the batteries with  $\text{MoS}_2/\text{MoO}_3$ -2 coated separators also achieved excellent cycling stability at  $1 \text{ C}$  and  $3 \text{ C}$ , with a low capacity decay rate of  $0.019\%$  per cycle after 1000 cycles (Figure S12) and  $0.025\%$  per cycle after 1000 cycles (Figure 6e, Table S3), respectively. Compared with many state-of-the-art reported separator coating materials, the  $\text{MoS}_2/\text{MoO}_3$ -2 displayed much better electrochemical performance (Table S4). To investigate the capacity contribution of  $\text{MoS}_2/\text{MoO}_3$  in LSBs, the battery with pristine  $\text{MoS}_2/\text{MoO}_3$ -2 cathode was assembled, and the charge/discharge measurement was performed at  $0.5 \text{ A g}^{-1}$ .

As displayed in Figure S13, the battery with  $\text{MoS}_2/\text{MoO}_3\text{-}2$  cathode had almost no charge/discharge plateaus and a negligible capacity compared with the LSBs.

The EIS spectra of the LSBs were further compared before and after 200 cycles. Before cycling, the Nyquist diagram of all  $\text{MoS}_2/\text{MoO}_3$  coated separators and pristine separator were composed of a semicircle and an inclined line (Figure 6f), related to the charge transfer resistance ( $R_{ct}$ ), and Warburg impedance ( $W_0$ ), respectively. However, another new semicircle appeared after cycling, which was associated with solid electrolyte interface ( $R_s$ ) film (Figure 6g). Compared with pristine separator and other modified separators, the LSBs with  $\text{MoS}_2/\text{MoO}_3\text{-}2$  coated separator had smaller  $R_{ct}$  before and after cycles (Table S5), indicating faster interfacial charge transfer.

The cycle stability of the LSBs with the  $\text{MoS}_2/\text{MoO}_3\text{-}2$  modified separators under higher sulfur loading were evaluated as well. As displayed in Figure 6h, the batteries could reach the initial capacities of 2.57, 3.39 and 4.0  $\text{mAh cm}^{-2}$  with different sulfur loading of 2.6, 3.8 and 5.2  $\text{mg cm}^{-2}$  at 0.5 C, respectively. The capacity could still maintain 686.5  $\text{mAh g}^{-1}$  (3.57  $\text{mAh cm}^{-2}$ ) after 100 cycles at 0.5 C under a high sulfur loading of 5.2  $\text{mg cm}^{-2}$ , with a low capacity decay rate of 0.11% per cycle, suggesting that  $\text{MoS}_2/\text{MoO}_3\text{-}2$  coating can efficiently suppress the lithium polysulfides shuttle. Furthermore, a Li-S coin battery with sulfur loading of 2.6  $\text{mg cm}^{-2}$  can power a LED light (inset of Figure 6h), indicating the good performance of  $\text{MoS}_2/\text{MoO}_3\text{-}2$  based LSBs.

## Conclusions

In summary, we synthesized amorphous  $\text{MoS}_2/\text{MoO}_3$  nanosheets by a one-step formamide (FA)-assisted strategy, which combines the advantages of high adsorption capability and good catalytic activity of  $\text{MoS}_2$ , and relatively high electronic conductivity and strong polarity of  $\text{MoO}_3$ . The existence of amorphous structures with abundant crystalline defects brought adequate active sites to anchor and catalyze LiPSs to inhibit LiPSs shuttling. The LSBs based on amorphous  $\text{MoS}_2/\text{MoO}_3\text{-}2$  nanosheets coated separators exhibit an outstanding specific capacity (1420.2  $\text{mA h g}^{-1}$  at 0.1 C), excellent rate capacity (505.4  $\text{mAh g}^{-1}$  at 5 C), and long cycle life (a negligible fading rate of 0.063% per cycle at 0.5 C). More importantly, the capacity could still maintain 686.5  $\text{mAh g}^{-1}$  (3.57  $\text{mAh cm}^{-2}$ ) after 100 cycles at 0.5 C under a high sulfur loading of 5.2  $\text{mg cm}^{-2}$ , with a low capacity decay rate of 0.11% per cycle. This work provides an idea for designing efficient amorphous catalytic materials in LSBs.

## Materials and Methods

### Preparation of the $\text{MoS}_2/\text{MoO}_3$ Samples

12 mmol of S (Aladdin) was dissolved in formamide (FA, 60 mL, Aladdin) solvent. After stirring for 15 min, a solution contains  $(\text{NH}_4)_6\text{Mo}_7\text{O}_{24}$  (2 mmol, Aladdin, S:Mo=1:1.2 (molar ratio) and FA (30 mL) solvent was introduced into the above solution and

maintained at 160 °C for 15 min. The products of  $\text{MoS}_2/\text{MoO}_3\text{-}2$  nanosheets were acquired by centrifugation, washed with ethanol and deionized water repeatedly, and then freeze-dried for 48 h. Similar, applying molar ratios of S and Mo of 2:1 and 1:2 can obtain  $\text{MoS}_2/\text{MoO}_3\text{-}1$  and  $\text{MoS}_2/\text{MoO}_3\text{-}3$ , respectively. The crystalline  $\text{MoS}_2/\text{MoO}_3$  was prepared by the hydrothermal method following a report except for the absence of RGO.<sup>[45]</sup>

## Characterizations

The morphologies and microstructures were determined by scanning electron microscope (SEM, GEMINI 500) and Transmission electron microscopy (TEM, Talos F200S). The crystalline phases and composition were examined by X-ray diffraction (XRD, Empyrean instrument with a Cu radiation), X-ray photoelectron spectra (XPS, Thermo Scientific K-Alpha), Raman spectra (Finder Vista). The UV-vis spectra were obtained using a SHIMADU UV-2600.

## Preparation of Modified Separator

$\text{MoS}_2/\text{MoO}_3\text{-}2$  nanosheets, acetylene black, and polyvinylidene fluoride (PVDF, Aladdin) were ground with 8:1:1 (mass ratio) in N-methyl-2-pyrrolidinone (NMP, Aladdin) solvent. Then the prepared slurry was coated on the Celgard 2400 (PP) separator. After vacuum drying at 55 °C for 12 h, the  $\text{MoS}_2/\text{MoO}_3\text{-}2$  nanosheets modified separator was obtained. Similar,  $\text{MoS}_2/\text{MoO}_3\text{-}1$ ,  $\text{MoS}_2/\text{MoO}_3\text{-}3$  nanosheets and crystalline  $\text{MoS}_2/\text{MoO}_3$  modified separators were prepared in the same way.

## Preparation of S/CNT Cathode

Sublimed sulfur and CNT were mixed with the sulfur proportion of 70 wt%, then sealed in a Teflon-lined autoclave and maintained at 155 °C for 12 h. After that, S/CNT composites were obtained. The obtained S/CNT, acetylene black and PVDF were ground with 8:1:1 (mass ratio) in NMP solvent to prepare slurry, then it was bladed on the one side of aluminum foil, in which the S loading was about 1.2~1.5  $\text{mg cm}^{-2}$ .

## Adsorption Test

3 mL  $\text{Li}_2\text{S}_6$  solution ( $\text{Li}_2\text{S}$  and S (1:5 by molar) dissolved in DOL/DME (1:1, vol.) solution) was added in a glass cuvette with 5 mg different  $\text{MoS}_2/\text{MoO}_3$  samples, and holding for 24 h for observation.

## Polysulfides Diffusion Test

A small bottle contained 2 mL 10 mM  $\text{Li}_2\text{S}_6$  solution was placed upside down in a large bottle with 10 mL DOL/DME solution, where the two different solutions were separated by different  $\text{MoS}_2/\text{MoO}_3$  modified separators, and holding for different time for observation.

## Electrochemical Measurements

CR2032 cells were fabricated in an Ar-filled glovebox ( $\text{H}_2\text{O}$ ,  $\text{O}_2$  <1 ppm) with lithium foil anodes, electrolyte (1 M LiTFSI dissolved in a 1,3-dioxolane and dimethoxymethane (1:1, vol.) with 0.1 M  $\text{LiNO}_3$ ), modified separator and sulfur cathodes (S/CNT). Galvanostatic discharge/charge performance was tested on a Neware battery tester. The cyclic voltammetry (CV),  $\text{Li}_2\text{S}$  nucleation/dissolution and electrochemical impedance spectroscopy (EIS, frequency: 0.1 Hz-100 kHz) were tested on an electrochemical workstation (Ivium N Stat).

## The Symmetric Cell Assembly

For symmetric cell, CR2032 coin cells were fabricated in an Ar-filled glovebox ( $\text{H}_2\text{O}$ ,  $\text{O}_2 < 1 \text{ ppm}$ ) with electrolyte (1 M LiTFSI dissolved in a 1,3-dioxolane and dimethoxymethane (1 : 1, vol.) with 0.1 M LiNO<sub>3</sub> and 0.25 M Li<sub>2</sub>S<sub>8</sub>), separator (Celgard 2400), two identical anodes and cathodes (MoS<sub>2</sub>/MoO<sub>3</sub> composites coated Al foil, loading: 1.0 mg cm<sup>-2</sup>).

## Lithium Nucleation and Decomposition

Lithium metal and Al foil loaded the different MoS<sub>2</sub>/MoO<sub>3</sub> composites were served as the anode and cathode, respectively. 10 μL Li–S electrolyte without Li<sub>2</sub>S<sub>8</sub> was added to the anode side and 10 μL Li<sub>2</sub>S<sub>8</sub> electrolyte (1 M LiTFSI dissolved in a tetraethylene glycol dimethyl with 0.2 M Li<sub>2</sub>S<sub>8</sub>) was added to the cathode side. The battery was discharged to 2.07 V at 0.112 mA, and the voltage was then switched to 2.02 V until the current dropped to 0.001 mA. To measure the decomposition of Li<sub>2</sub>S are similar. Firstly, the battery was charged to 1.7 V at 0.112 mA, and then the voltage was switched to 2.4 V until the current dropped to 0.001 mA.

## Acknowledgements

This research gets financial support from the Doctor Foundation of China West Normal University (21E049), the Science and Technology of Sichuan Province (2022NSFSC0261), the Opening Project of Material Corrosion and Protection Key Laboratory of Sichuan province (2022CL24), and the National Research Foundation of China (21571148).

## Conflict of Interests

The authors declare no competing financial interest.

## Data Availability Statement

The data that support the findings of this study are available in the supplementary material of this article.

**Keywords:** One-step FA-assisted strategy · Amorphous MoS<sub>2</sub>/MoO<sub>3</sub> nanosheets · Abundant active sites · Lithium-sulfur batteries

- [1] L. Luo, S. H. Chung, A. Manthiram, *J. Mater. Chem. A* **2018**, *6*, 7659–7667.
- [2] N. N. Wang, Y. X. Wang, Z. C. Bai, Z. W. Fang, X. Zhang, Z. F. Xu, Y. Ding, X. Xu, Y. Du, S. X. Dou, G. H. Yu, *Energy Environ. Sci.* **2020**, *13*, 562–570.
- [3] G. M. Zhou, H. Chen, Y. Cui, *Nat. Energy* **2022**, *7*, 312–319.
- [4] M. X. Fang, Q. G. Huang, L. B. Ma, J. Xu, Q. Kang, Y. J. Cao, S. Z. Hu, X. S. Zhang, D. F. Niu, *Electrochim. Acta* **2022**, *434*, 141301.
- [5] J. Xu, F. T. Yu, J. L. Hua, W. Q. Tang, C. Yang, S. Z. Hu, S. L. Zhao, X. S. Zhang, Z. Xin, D. F. Niu, *Chem. Eng. J.* **2020**, *392*, 123694.
- [6] R. X. Wang, K. L. Wang, H. W. Tao, W. J. Zhao, M. Jiang, J. Yan, K. Jiang, *J. Mater. Chem. A* **2020**, *8*, 11224–11232.
- [7] S. J. Fretz, M. Agostini, P. Jankowski, P. Johansson, A. Matic, A. E. C. Palmqvist, *Batteries & Supercaps* **2020**, *3*, 757–765.
- [8] S. X. Jiang, M. F. Chen, X. Y. Wang, P. Zeng, Y. F. Li, H. Liu, X. L. Li, C. Huang, H. B. Shu, Z. G. Luo, C. Wu, *Electrochim. Acta* **2019**, *313*, 151–160.
- [9] W. Liu, C. Luo, S. W. Zhang, B. Zhang, J. B. Ma, X. L. Wang, W. H. Liu, Z. J. Li, Q. H. Yang, W. Lv, *ACS Nano* **2021**, *15*, 7491–7499.
- [10] P. Wang, B. J. Xi, Z. C. Y. Zhang, M. Huang, J. K. Feng, S. L. Xiong, *Angew. Chem. Int. Ed.* **2021**, *60*, 15563–15571.
- [11] X. Fang, H. S. Peng, *Small* **2015**, *11*, 1488–1511.
- [12] C. H. Chang, S. H. Chung, A. Manthiram, *Small* **2016**, *12*, 174–179.
- [13] S. H. Chung, A. Manthiram, *Adv. Mater.* **2014**, *26*, 7352–7357.
- [14] J. Balach, T. Jaumann, M. Klose, S. Oswald, J. Eckert, L. Giebel, *J. Power Sources* **2016**, *303*, 317–324.
- [15] F. Pei, L. L. Lin, A. Fu, S. G. Mo, D. H. Ou, X. L. Fang, N. F. Zheng, *Joule* **2018**, *2*, 323–336.
- [16] M. L. Jana, R. Xu, X. B. Cheng, J. S. Yeon, J. M. Park, J. Q. Huang, Q. Zhang, H. S. Park, *Energy Environ. Sci.* **2020**, *13*, 1049–1075.
- [17] J. Zhang, W. Z. Ma, Z. Y. Feng, F. F. Wu, D. H. Wei, B. J. Xi, S. L. Xiong, *J. Energy Chem.* **2019**, *39*, 54–60.
- [18] Y. B. Yang, H. Xu, S. X. Wang, Y. F. Deng, X. Y. Qin, X. S. Qin, G. H. Chen, *Electrochim. Acta* **2019**, *297*, 641–649.
- [19] Y. Z. Song, S. Y. Zhao, Y. R. Chen, J. S. Cai, J. Li, Q. H. Yang, J. Y. Sun, Z. F. Liu, *ACS Appl. Mater. Interfaces* **2019**, *11*, 5687–5694.
- [20] W. J. Qiu, C. H. An, Y. W. Yan, J. Xu, Z. J. Zhang, W. Guo, Z. Wang, Z. J. Zheng, Z. B. Wang, Q. B. Deng, J. S. Li, *J. Power Sources* **2019**, *423*, 98–105.
- [21] T. X. Tan, N. N. Chen, Z. K. Wang, Z. M. Tang, H. R. Zhang, Q. X. Lai, Y. Y. Liang, *ACS Appl. Energ. Mater.* **2022**, *5*, 6654–6662.
- [22] S. X. Jiang, M. F. Chen, X. Y. Wang, Z. Y. Wu, P. Zeng, C. Huang, Y. Wang, *ACS Sustainable Chem. Eng.* **2018**, *6*, 16828–16837.
- [23] B. S. Guo, S. Bandaru, C. L. Dai, H. Chen, Y. Q. Zhang, J. J. Xu, S. J. Bao, M. Y. Chen, M. W. Xu, *ACS Appl. Mater. Interfaces* **2018**, *10*, 43707–43715.
- [24] X. Y. Shi, L. W. Yang, S. Li, Y. Wang, X. Y. Chen, Z. G. Wu, Y. J. Zhong, Y. X. Chen, S. Y. Gao, G. K. Wang, X. D. Guo, B. H. Zhong, *Electrochim. Acta* **2021**, *390*, 138829.
- [25] J. Pu, T. Wang, X. M. Zhu, Y. Tan, L. Gao, J. X. Chen, J. R. Huang, Z. H. Wang, *Electrochim. Acta* **2022**, *435*, 141396.
- [26] B. Moorthy, S. Kwon, J. H. Kim, P. Ragupathy, H. M. Lee, D. K. Kim, *Nanoscale Horiz.* **2019**, *4*, 214–222.
- [27] L. B. Ma, G. Y. Zhu, W. J. Zhang, P. Y. Zhao, Y. Hu, Y. R. Wang, L. Wang, R. P. Chen, T. Chen, Z. X. Tie, J. Liu, Z. Jin, *Nano Res.* **2018**, *11*, 6436–6446.
- [28] Y. M. Gao, S. Y. Liu, J. D. Zhang, X. Y. Chen, B. Han, Y. L. Wang, J. H. Guo, Z. S. Jin, J. J. Li, X. D. Meng, *Dalton Trans.* **2023**, *52*, 16513–16518.
- [29] L. P. Wu, C. Y. Cai, X. Yu, Z. H. Chen, Y. X. Hu, F. Yu, S. J. Zhai, T. Mei, L. Yu, X. B. Wang, *ACS Appl. Mater. Interfaces* **2022**, *14*, 35894–35904.
- [30] J. Wu, Q. G. Feng, Y. C. Wang, J. X. Wang, X. Zhao, L. S. Zhan, M. J. Liu, Z. Q. Jin, Z. Y. Chen, Y. P. Lei, *Chem. Commun.* **2023**, *59*, 2966–2969.
- [31] S. Yang, J. F. Zhang, T. Z. Tan, Y. Zhao, N. Liu, H. P. Li, *Materials* **2018**, *11*, 2064.
- [32] D. Lei, W. Z. Shang, X. Zhang, Y. P. Li, X. S. Shi, S. M. Qiao, Q. Wang, Q. Zhang, C. Hao, H. Xu, G. H. Chen, G. H. He, F. X. Zhang, *J. Energy Chem.* **2022**, *73*, 26–34.
- [33] Z. A. Ghazi, X. He, A. M. Khattak, N. A. Khan, B. Liang, A. Iqbal, J. X. Wang, H. S. Sin, L. S. Li, Z. Y. Tang, *Adv. Mater.* **2017**, *29*, 1606817.
- [34] N. Zheng, G. Y. Jiang, X. Chen, J. Y. Mao, N. Jiang, Y. S. Li, *Nano-Micro Lett.* **2019**, *11*, 1–15.
- [35] J. Yu, J. W. Xiao, A. R. Li, Z. Yang, L. Zeng, Q. F. Zhang, Y. J. Zhu, L. Guo, *Angew. Chem. Int. Ed.* **2020**, *59*, 13071–13078.
- [36] J. H. Xiao, J. S. Lv, Q. F. Lu, *Mater. Lett.* **2022**, *311*, 131580.
- [37] M. Liaqat, N. R. Khalid, *Appl. Nanosci.* **2021**, *11*, 2085–2094.
- [38] M. Szkoda, K. Trzciński, M. Lapinski, *Electrocatalysis* **2020**, *11*, 111–120.
- [39] Y. L. Zhu, Y. T. Tan, H. B. Li, *J. Energy Storage* **2023**, *60*, 106657.
- [40] Y. F. Niu, H. G. Su, X. L. Li, J. Li, Y. X. Qi, *J. Alloys Compd.* **2022**, *898*, 162863.
- [41] X. Wu, S. X. Zhao, L. Q. Yu, J. W. Li, E. L. Zhao, C. W. Nan, *Electrochim. Acta* **2019**, *297*, 872–878.
- [42] X. J. Wang, R. Nesper, C. Villevieille, P. Novák, *Adv. Energy Mater.* **2013**, *3*, 606–614.
- [43] Z. B. Chen, D. Cummins, B. N. Reinecke, E. Clark, M. K. Sunkara, T. F. Jaramillo, *Nano Lett.* **2011**, *11*, 4168–4175.
- [44] S. Z. Deng, Y. C. Yan, L. Q. Wei, T. Li, X. Su, X. J. Yang, Z. T. Li, M. B. Wu, *ACS Applied Energy Materials* **2019**, *2*, 1266–1273.
- [45] D. Lei, W. Z. Shang, X. Zhang, Y. P. Li, S. M. Qiao, Y. P. Zhong, X. Y. Deng, X. S. Shi, Q. Zhang, C. Hao, X. D. Song, F. X. Zhang, *ACS Nano* **2021**, *15*, 20478–20488.
- [46] H. Zhang, G. Q. Shen, X. Y. Liu, B. Ning, C. X. Shi, L. Pan, X. W. Zhang, Z. F. Huang, J. J. Zou, *Chin. J. Catal.* **2021**, *42*, 1732–1741.

- [47] I. D. Silva, A. C. Reinaldo, F. A. Sigoli, I. O. Mazali, *RSC Adv.* **2020**, *10*, 18512–18518.
- [48] B. C. Windom, W. G. Sawyer, D. W. Hahn, *Tribol. Lett.* **2011**, *42*, 301–310.
- [49] J. Li, S. Hou, T. Z. Liu, L. K. Wang, C. Mei, Y. Y. Guo, L. Z. Zhao, *Chem. Eur. J.* **2020**, *26*, 2013–2024.
- [50] M. J. Shao, H. W. Sheng, L. Q. Lin, H. Y. Ma, Q. Wang, J. Yuan, X. T. Zhang, G. Chen, W. Q. Li, Q. Su, E. R. Xie, J. Wang, Z. B. Zhang, W. Lan, *Small* **2023**, *19*, 2205529.
- [51] J. F. Wang, J. Li, *J. Colloid Interface Sci.* **2022**, *616*, 298–303.
- [52] A. Ashok, A. Kumar, J. Ponraj, S. A. Mansour, *Carbon* **2020**, *170*, 452–463.
- [53] C. Y. Xu, W. Lu, L. Yan, J. Q. Ning, C. C. Zheng, Y. J. Zhong, Z. Y. Zhang, Y. Hu, *J. Colloid Interface Sci.* **2020**, *562*, 400–408.
- [54] J. L. Yan, Y. Y. Wang, C. Yang, H. Y. Deng, N. T. Hu, *J. Alloys Compd.* **2024**, *976*, 173208.
- [55] X. Y. Tao, J. G. Wang, C. Liu, H. T. Wang, H. B. Yao, G. Y. Zheng, Z. W. Seh, Q. X. Cai, W. Y. Li, G. M. Zhou, C. X. Zu, Y. Cui, *Nat. Commun.* **2016**, *7*, 11203.
- [56] Z. Y. Han, S. Y. Zhao, J. W. Xiao, X. W. Zhong, J. Z. Sheng, W. Lv, Q. F. Zhang, G. M. Zhou, H. M. Cheng, *Adv. Mater.* **2021**, *33*, 2105947.

Manuscript received: February 7, 2024

Revised manuscript received: April 2, 2024

Accepted manuscript online: May 19, 2024

Version of record online: June 27, 2024